



Experiments on cold-formed steel Zee-shaped stub beam-columns

Shahabeddin. Torabian¹, David .C. Fratamico², Benjamin.W. Schafer³

Abstract

As a part of studies on the structural strength and stability of cold-formed steel beam-columns, twenty-two structural Zee sections at a length of 305 mm were tested under several load combinations of biaxial bending moments and axial force. Differences between Zees (tested in this 2nd phase of the work) and lipped C-channels (tested previously in Phase 1) such as the location of the principal axes and the shear center could provide a means to evaluate the behavior of beam-columns in a more general way. The short length of the specimens was utilized to mobilize local buckling and avoid distortional and global buckling phenomena. The combined axial force and biaxial bending moments were applied via a special test rig designed to apply axial load with eccentricities. The results were used to evaluate the reliability of the current AISI-S100-12 specification for beam-column strength prediction via both effective width and direct strength methods. Both methods employ a simple linear interaction equation for strength prediction of the members under combined actions. The experimental results showed a considerable prospective for improvement in the current specification approach and providing more optimized and realistic results in design. Accordingly, the potentials for further improvements of the direct strength design method for cold-formed steel beam-columns are discussed.

1. Introduction

To continue the studies on the structural strength and stability of cold-formed steel beam-columns at Johns Hopkins University (Torabian et. al. 2013, 2014a, 2014b, 2015), structural Zee sections are considered in Phase 2 of the experimental program to evaluate the behavior of beam-columns in a more general way. Zee sections are a commonly employed cross-section in metal buildings serving as purlins and girts (see Fig. 1). Although purlins and girts are often designed for transverse loading demands (i.e. gravity, live, snow, wind, etc.), integrated behavior of the steel frames such as diaphragm action can subject roof purlins and longitudinal girts to an axial force along with the bending moment already induced by the transverse loadings. Therefore, structural Zee sections do have occasions where they must be designed as beam-columns subjected to axial forces and bending moments.

¹ Assistant Research Scientist, Department of Civil Engineering, Johns Hopkins University, <torabian@jhu.edu>
School of Civil Engineering, College of Engineering, University of Tehran, Tehran, Iran, <torabian@ut.ac.ir>

² Graduate Research Assistant, Department of Civil Engineering, Johns Hopkins University, <fratamico@jhu.edu>

³ Professor and Chair, Department of Civil Engineering, Johns Hopkins University, <schafer@jhu.edu>

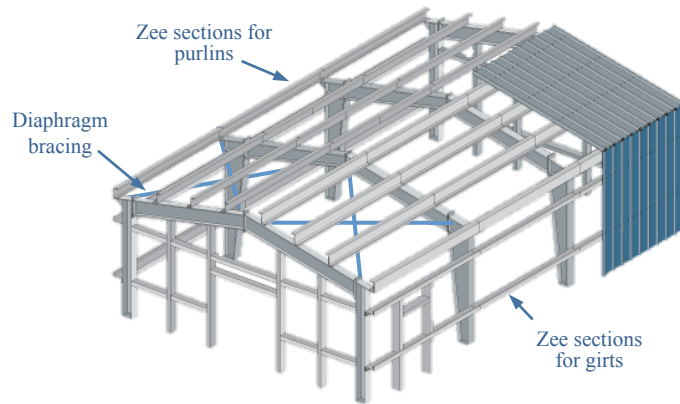


Figure 1: Applications of Zee sections in steel frame buildings (Prime 2015 with annotations)

Differences between Zees and lipped C-channels (tested in Phase 1 of the research) such as the location of the principal axes with respect to the geometrical axes (see Table 1), and the location of shear center suggest that it may be advantageous to examine the behavior of beam-columns in a more general way. Accordingly, Zee sections were tested in Phase 2 of the research program under several load combinations of biaxial bending moments and axial force.

Table 1: Bending stress distribution in geometrical/constrained and principal axis bending in Zee sections

	Geometric/Constrained axes bending		Principal axes bending	
	M_{zz} (major) ^a	M_{xx} (minor)	M_{11} (major)	M_{22} (minor)
Applied moment				
Bending stress distribution				

^a Red stress shows compressive bending stress and blue stress shows tensile bending stress

In Phase 1 of the project, the failure modes and the member capacity of fifty-five 600S137-54 (AISI-S200-12 nomenclature) lipped channel beam-column sections under combined bi-axial bending moments and axial force were characterized by testing the specimen with three different lengths: 305 mm (short), 610 mm (intermediate), and 1219 mm (long). It was found that the predictions of both the effective width method (EWM) and direct strength method (DSM) in the current AISI-S100-12 are conservative for lipped channel beam-column and improvements should be sought (Torabian et. al. 2014a, 2015). The previous studies connected the

conservatism of the current design methods to ignoring the nonlinear interaction of the applied load actions by utilizing a simple interaction equation for beam-column strength predictions. As the stability of the cross-section (i.e. local and distortional buckling capacities) is strongly tied to the stress distribution, the realistic cross-section stability cannot be seen by simple interaction equations (Torabian et. al. 2015).

Along with the extensive efforts on determining the capacity of cold-formed steel members under pure axial or flexural actions (referred as anchor points herein), the design of structural members under combination of axial force and bending moments needs more comprehensive experimental research work, although previous work does exist in the literature (Loh 1985, Pekoz 1986, Miller and Pekoz 1994, Kalyanaraman and Jayabalan 1994, Yiu and Pekoz 2000, Shifferaw 2010). However, for the particular case of Zee beam-column sections, experimental studies are rare.

In this paper, twenty-two 700Z225-60 (similar to AISI-S200-12 nomenclature) Zee shaped stub beam-column sections are tested under combined bi-axial bending moments and axial force to characterize the failure modes and the member strength. The loadings were applied via a test rig designed to apply eccentric axial load. A reliability-based method is utilized to evaluate the strength prediction of the current specification via both effective width and direct strength methods and the potential for further improvement of the current specification for predicting the strength of cold-formed steel beam-columns is discussed.

This study is the experimental part of Phase 2 of an ongoing comprehensive study on DSM prediction for cold-formed steel beam-columns (Torabian et. al. 2013 and 2015). Both Phases of the study include finite element collapse analyses, parametric analysis on different sizes of the cross-sections, and reliability assessment of the current and the new strength prediction methods. The result are being used to develop an explicit new design formulation that takes into account the cross-section stress distribution under combined actions.

2. Experimental Program

2.1 Test Matrix

To define the applied combined actions in the test matrix including bi-axial bending moments (M_1 , M_2) and axial force (P), a non-dimensionalized cylindrical coordinate system is implemented using coordinates θ_{MM} , ϕ_{PM} , β . Points in the normalized P - M_1 - M_2 space are defined by an azimuth angle, $\theta_{MM} = \tan^{-1}(y/x)$, an elevation angle, $\phi_{PM} = \cos^{-1}(z/\beta)$, and a radial length $\beta = \sqrt{x^2 + y^2 + z^2}$, where $x = M_1/M_{1y}$ (principal major-axis bending), $y = M_2/M_{2y}$ (principal minor-axis bending), and $z = P/P_y$ (See Torabian et. al. 2013 and 2015 for further explanations, also note β in this context has nothing to do with reliability).

The points corresponding to the strength of a beam-column member under different combinations of bi-axial bending moments (M_1 , M_2) and axial force (P) create a strength surface in the normalized P - M_1 - M_2 space. Building this surface experimentally requires many tests and practically only a limited number of tests may be completed. Therefore, consistent with Phase 1 of this study, a single Zee section under a variety of load conditions and different lengths is considered to investigate different modes of failure.

The selected Zee cross-section in this study is the 700Z225-60 Zee (purlin) with $F_y=550\text{MPa}$ (similar to AISI-S200-12 nomenclature). The selected specimens are short (305 mm) to elevate (brace) distortional and global buckling modes and allow the local buckling mode to develop. The distortional buckling half-wavelength is 585 mm, which is more than the length of the specimen. Moreover, as the specimens are welded to the end plates before being set in the beam-column test rig, the specimen has warping fixed ends, which results in a significant boost above its simply-supported value (based on the signature curve) and as a result, local buckling becomes the primary mode for the stub beam-columns.

Table 2: Test Matrix

Loading condition		Short specimens (L=305mm)					
No.	θ_{MM}^a (deg.)	Test specimen Z700-12-	ϕ_{PM}^a (deg.)	e_{x-m}^b (mm)	e_{z-m}^b (mm)	θ_{MM-m}^b (deg.)	ϕ_{PM-m}^b (deg.)
1	Minor axis bending	1	25.0	-1.5	-4.3	277.1	24.0
2		2	50.0	-4.1	-11.4	277.3	49.3
3		3	81.0	-21.8	-62.8	277.0	81.3
4		22 ^c	81.0	-21.2	-61.2	277.0	81.0
5		21 ^d	83	-22.8	-61.9	89.9	83.0
6		4 ^d	60	-17.9	-9.6	81.9	61.8
7		5 ^d	77	-46.8	-22.2	80.9	77.5
8		6 ^d	85	-135.4	-68.9	81.4	85.8
9	Major axis/ Geometric Major axis bending	7	30.0	-28.1	-10.5	352.2	30.2
10		8	55.0	-70.3	-24.5	1.3	55.1
11		9	75.0	-183.1	-63.7	0.8	75.0
12		19 ^e	55.0	-69.6	-22.5	5.1	54.7
13		20 ^e	75.0	-183.0	-58.7	9.7	75.1
14	Bi-axial bending	10	40.0	-35.6	-9.2	25.4	38.0
15		11	75.0	-163.3	-39.0	30.9	75.1
16		12	40.0	-21.7	-1.5	60.1	39.0
17		13	75.0	-99.8	-7.3	59.8	74.9
18		14	40.0	-19.1	-12.5	301.7	39.0
19		15	75.0	-82.8	-56.1	300.5	74.7
20		16	40.0	-34.6	-15.7	327.0	41.0
21	17	75.0	-155.2	-68.0	330.4	75.0	
22	Column	18	0.0	-0.8	0.2	77.8	3.4

^a Target angle

^b Measured angle

^c Similar to Z700-12-3

^d Due to the loading rig limitations, these specimens should be tested upside-down.

^e Geometric Major axis ($\theta_{MM}=8\text{ deg.}$)

In the non-dimensionalized cylindrical coordinates (θ_{MM} , ϕ_{PM} , β) for the normalized P - M_1 - M_2 space, twenty-two load combinations are selected for testing. As tabulated in Table 2, thirteen specimens are considered for principal axes bending and axial force, including minor-axis bending (no. 1-8, $\theta_{MM}=90^\circ$ and 270°), as well as major-axis and geometric/constrained axis bending (no. 9-13, $\theta_{MM}=0^\circ$ and 8°). Eight other specimens (no. 14-21) are considered in four other non-principal axes with bi-axial bending and axial force ($\theta_{MM} = 30^\circ, 60^\circ, 300^\circ, 330^\circ$) and one additional test (no. 22) was conducted in pure axial compression. It should be noted, that the selected azimuth angles cover both principal and constrained axis bending conditions as explained in Table 1. The greater number of specimens assigned to minor-axis bending follows the Phase 1 results that had considerably high test-to-predicted ratios due to high inelastic reserve capacity in the lippled channel specimens.

Each specimen in the experimental program has a designation of $Z700$ - L - X , where the 700 indicates the depth (in inches $\times 100$, i.e., the same as the AISI-S200-12 nomenclature), L is the length of the specimen in inches, and X is a sequential number assigned before testing, which is not necessarily consistent with the assigned identification number (abbreviated no.). Table 2 provides targeted angles and also the actual loading angles calculated based on the averaged measured initial eccentricities of the specimen before testing. More detailed loading conditions, and the equivalent physical eccentricities used in the tests are tabulated in Table 2 (see Fig. 3(b) for the definition of the x and z). The coordinate system used in the physical testing (Fig. 3(b)) is not to be confused with the generalized coordinate system in the normalized P - M_1 - M_2 coordinate system.

Table 3: Tensile test results: Coupon test results

No.	Specimen ^a	Uncoated thickness	Elongation (50 mm gage length)	Upper Yield strength	Yield strength (0.2% offset)	Yield strength (ave. 0.4% to 0.8%)	Yield point strain	Tensile strength	Strain at Tensile strength	Strain at rupture
		t_{uc} (mm)	e (50 mm gage) (%)	F_{UYS} (MPa)	F_y (0.2% offset) (MPa)	F_y (0.4 to 0.8%) (MPa)	ϵ_y (mm/mm)	F_u (MPa)	ϵ_u (mm/mm)	ϵ_r (mm/mm)
1	700-12-1-W	1.50	19.8%	559.2	542.6	542.2	0.0190	581.4	0.13	>0.2 ^b
2	700-12-1-F-(L)	1.48	20.0%	569.3	552.2	549.7	0.0193	595.2	0.12	>0.14 ^b
3	700-12-1-F-(R)	1.51	19.7%	549.1	542.4	542.5	0.0186	580.6	0.12	>0.14 ^b
4	700-12-2-W	1.49	20.4%	554.1	547.2	546.3	0.0188	579.4	0.14	>0.2 ^b
5	700-12-2-F-(L)	1.47	19.1%	554.4	551.1	552.4	0.0188	589.6	0.13	>0.2 ^b
6	700-12-2-F-(R)	1.50	21.9%	553.6	539.9	540.6	0.0188	579.2	0.15	>0.2 ^b
7	700-48-1-W	1.50	14.3%	556.6	550.9	550.6	0.0189	584.7	0.13	0.13 ^c
8	700-48-1-F-(L)	1.46	13.8%	570.5	562.5	561.1	0.0193	604.4	0.12	0.12 ^c
9	700-48-1-F-(R)	1.51	12.0%	569.9	570.0	571.7	0.0193	584.2	0.08	0.09 ^c
10	700-48-2-W	1.49	14.2%	559.0	546.7	547.0	0.0189	580.6	0.13	0.13 ^c
11	700-48-2-F-(L)	1.48	18.5%	563.0	558.1	557.5	0.0191	596.4	0.13	>0.2 ^b
12	700-48-2-F-(R)	1.52	20.4%	549.0	542.5	541.9	0.0186	579.4	0.13	>0.14 ^b
				Mean	550.5	550.3		586.2		
				COV	1.7%	1.7%		1.4%		

^a 700-L-N-S (700: depth of specimen, L: Length, N: Number, S: Specimen location, web (W), Left (L) or Right (R) Flange (F))

^b Max extensometer strain is 0.2. note: extensometer slipped earlier for some coupons.

^c Ruptured outside of the 50mm gage length.

2.2 Test specimens, preparation and material testing

Test specimens consisted of Zee sections with 0.75 in. thick end plates, which can provide warping fixed restraints and enable the specimen to be placed in the rig and clamped to the loading plates, as shown in Fig. 3. To estimate the realistic shape of the test specimen cross-section dimensions such as depth (H), flange width (B), lip length (d) and the corner angles and radii were measured manually before welding. After preparing the specimens by milling the ends, and stripping the zinc coating of the end edges, the Zee specimens were welded to the end plate with a minimal weld size of 3mm to avoid end plate deformation. Welding was visually inspected to ensure a complete and sound connection between the specimen and the end plate, and are generally regarded to be of excellent quality.

Twelve tensile coupons were sampled from the web and flanges of the specimens in accordance to ASTM A370-12a (A370-12a 2012), as tabulated in Table 3. The tensile test results are provided in Table 3. Average yield and ultimate strengths were determined and the averaged engineering stress-strain curve ($\sigma_E-\epsilon_E$) is provided in Fig. 2 along with the coupon test dimensions. In these tests, the Young's modulus was not measured directly and a nominal Young's modulus of 203 MPa is adopted according to AISI-S100-12 (AISI-S100 2012).

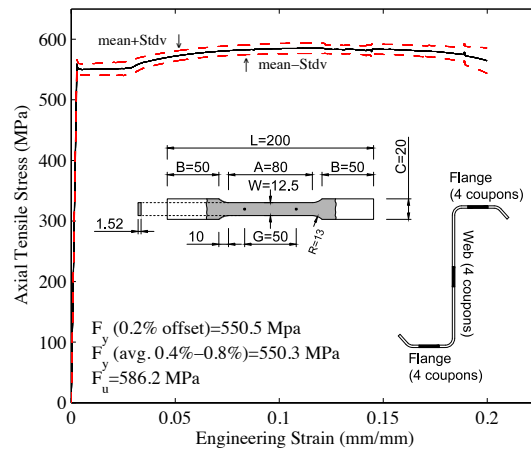
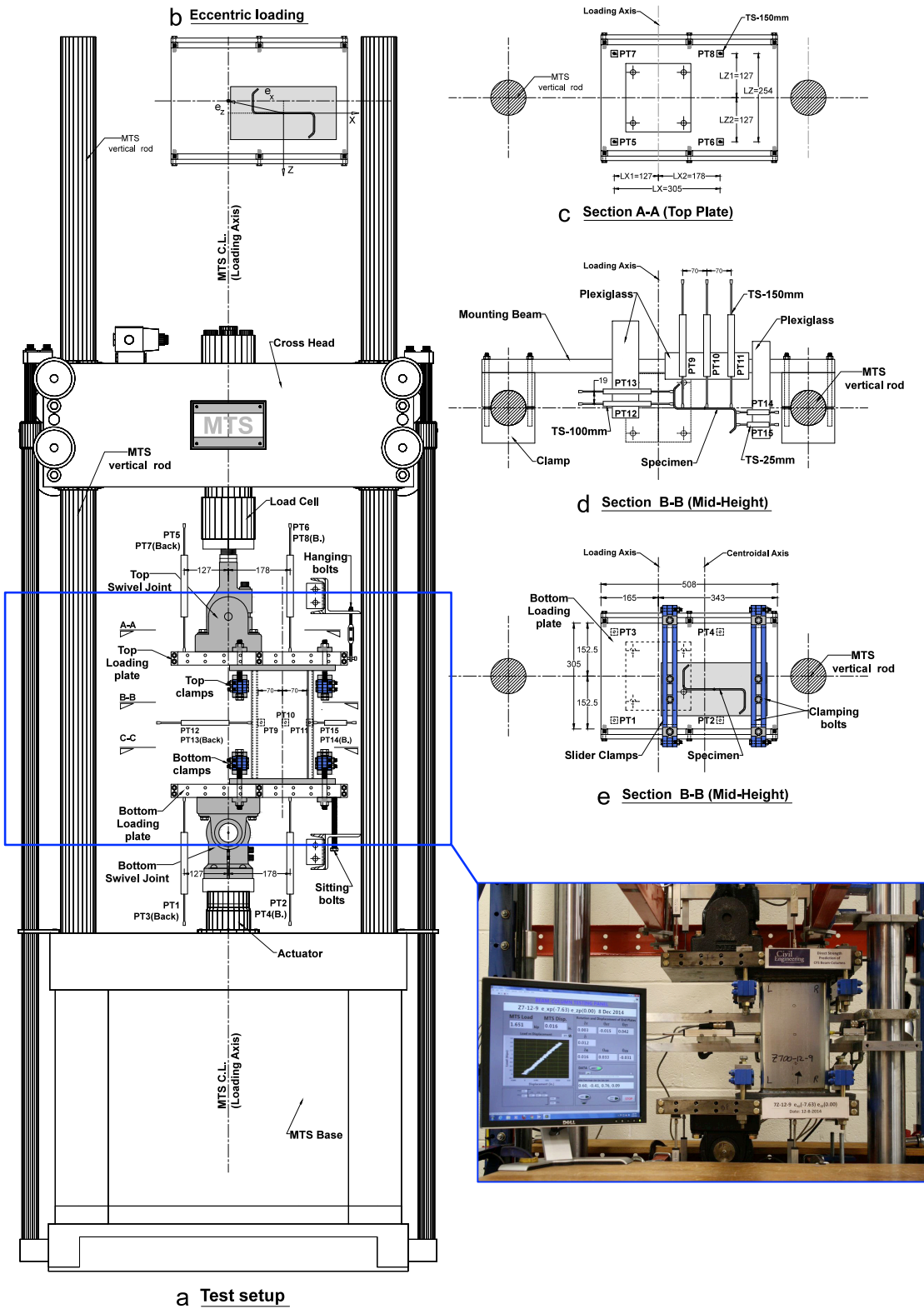


Figure 2: Tensile test results: Average engineering stress-strain curve

2.3 Test setup, instrumentation, and the loading equipment

The test rig and the instrumentation configuration designed in Phase 1 of the experimental program, which was on the lipped channels (Torabian et. al. 2015), has been utilized to pursue the experiments in Phase 2. As shown in Fig. 3, the test rig consists of a uniaxial 445 kN MTS loading frame, top and bottom MTS standard swivel joints for providing pin-pin end-restraints, two loading plates to accommodate eccentricity in both axes, required clamps, instrumentation, and a data acquisition system.

Eight position transducers (abbreviated as PTs, herein) mounted on the top and bottom loading plates were utilized to record rotations and displacements of these plates (see Fig. 3(c) and (e)), and seven other PTs were utilized to record the movements and deformations of the specimen at mid-height, as shown in Fig. 3(d). These PTs measured the cross-section movements at 7 points including both flanges and the web. Examples of the recorded cross-sectional deformation are shown in Table 4 and are discussed later in the paper.



2.4 Specimen placement and testing procedure

Providing the initial eccentricities for specimens is an important step in the testing procedure. To measure the position of the Zee specimens, three precise reference measuring beams (the middle one named as the mounting beam) were utilized as shown in Fig. 4. The ruler on the top and bottom measuring beams measures the position of the specimens in the x direction (d_{xT} : top ruler, d_{xB} : bottom ruler), and a caliper measures eccentricities in the z direction at four points (d_{zT} : top ruler, d_{zB} : bottom ruler, $d_{MI, z}$: mounting beam). The measured initial eccentricities are tabulated in Table 2, along with the corresponding azimuth and elevation angles (θ_{MM-m} , ϕ_{PM-m}). After placing the specimens in the rig, all tests were performed monotonically in displacement control with a proper loading rate (typically 0.0025-0.0035 mm/sec.) up to the maximum load capacity and then continued to more than 20% strength degradation before stopping the test.

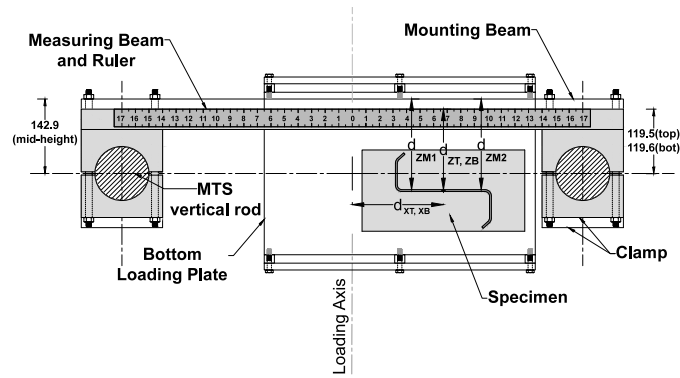


Figure 4: Setting the specimens in the test rig (top measuring beam and mounting beam (see Fig. 3))

2.5 Test results and observations

The maximum axial load capacity of the specimens, P_{max} , along with the failure picture and the cross-sectional deformation at the mid-height of the specimen are provided in Table 4. Moreover, Table 5 provides the normalized radial length, β_{Test} , and the corresponding azimuth and elevation angles at the failure point (θ_{MM-f} , ϕ_{PM-f}). Notably, due to the fact that the load is applied to a pin about which the end plate rotates (and where P is applied or reacted) is 158 mm from the end of the specimens, the measured top and bottom plate rotations can provide additional eccentricities to the measured initial values tabulated in Table 2. Accordingly, the peak moments used to calculate (β_{Test} , θ_{MM-f} , ϕ_{PM-f}) in Table 5 account for the exact end eccentricity resulted from the initial eccentricities and the effect of end plate rotations.

The characteristic observed failure mode of the first eight specimens (no. 1-8), which are mostly under axial force and principal minor-axis bending, was local buckling predominately in the web (WLB) close to the flange in tension and local/distortional flange buckling FLB/FDB of the flange in compression, as shown in Table 4(a). Following the web buckling, flange deformations aligned with WLB was observed in all tests. Similarly, following the flange buckling, web deformations consistent with the FLB/FDB buckling were observed. In almost all specimens, the flange lip of the Zee section was the common place of buckling initiation, but after lip buckling and mostly inward deformation of the flange under compression, the failure (a plastic mechanism) occurs in the web approximating WLB permanent deformations and in the

compressive flange as FLB/FDB permanent deformations. The observed buckling pattern can be understood by the stress distribution provided in Table 1 for the case of principal minor-axis bending. While the principal minor-axis (axis 2) of the Zee cross-section passes through the flanges, the minor-axis bending can cause compressive stress on the lip of one flange and on the flange-web corner of the other flange. Test observations showed the buckling pattern of the specimens followed the compressive stress distribution over the cross section.

Table 4: Test results: Specimens at maximum strength and the cross-sectional deformation at the mid-height

(a)		Axial force and Minor axis bending							
Spec. No. ^a		(1)	(2)	(3)	(4)	(5)	(6)	(7)	(8)
Test Specimen at the failure load									
P_{max} (kN)		109.8	92.8	37.0	32.3	31.5	79.7	49.7	21.3
Cross-section ^b deformation									
(b)		Axial force and Major axis bending					Axial force		
Spec. No. ^a		(9)	(10)	(11)	(12)	(13)	(22)		
Test Specimen at the failure load									
P_{max} (kN)		93.1	68.2	34.7	72.1	39.4	131.8		
Cross-section deformation									
(c)		Axial force and Bi-axial bending							
Spec. No. ^a		(14)	(15)	(16)	(17)	(18)	(19)	(20)	(21)
Test Specimen at the failure load									
P_{max} (kN)		93.8	42.8	109.8	55.0	88.8	43.1	83.9	34.3
Cross-section deformation									

^a For specimen numbers and more details see Table-2.

^b blue: undeformed shape, cyan: 0.25 P_{max} , green: 0.5 P_{max} , yellow: 0.75 P_{max} , red: P_{max} , orange: 0.85 P_{max} -post peak

Under axial load and principal major-axis bending (no. 9-11), web local buckling (WLB) was the dominant buckling mode accompanied by a local/distortional flange buckling FLB/FDB of the compressive flange as shown in Table 4(b). Buckling typically occurred on the “left side” (the side with compression from major-axis moment), and in all cases consistent deformation of the web and the adjacent flange was observed. In the two specimens (no. 12-13), tested under axial

load and constrained major-axis bending (see Table 1 for the stress distribution) the observed failure modes were similar to the principal major-axis bending specimens. As observed in the first eight specimens, test observations of the beam-column specimens having axial force and major-axis bending also showed high correlation between the compressive stress distribution over the cross section and the buckled shape of the specimens.

The remaining specimens were tested under axial load and bi-axial bending. Four specimens have applied axial compression, major-axis bending, and positive minor-axis bending (no. 14-17); and four other specimens (no. 18-21) have applied axial compression, major-axis bending, and negative minor-axis bending. For no. 14-17 all loading adds to the compressive stress on the flange-web corner, making web local buckling (WLB) the main failure mode for all four specimens at $\theta_{MM}=30^\circ$ and 60° (see Table 4(c)). For no. 18-21 at $\theta_{MM}=300^\circ$ and 330° the observed failure mode was flange local/distortional buckling FL/DB. Following the flange buckling, web deformation aligned with the FL/DB buckling shapes was observed in all four tests. The more pronounced flange buckling of the specimens at $\theta_{MM}=300^\circ$ and 330° compared to the specimens $\theta_{MM}=30^\circ$ and 60° are shown in terms of the deformed shapes in Table 4(c).

In most specimens, lip buckling initiated first and followed by a flange distortional deformation. Accordingly, the buckling shape of the flange might be described as local buckling and distortional deformation that ended up in a permanent local buckling shape in the flange as shown in Fig. 5. This type of buckling is named as local/distortional flange buckling (FL/DB), herein. Consistent to the stress distribution over the cross-section, the web buckling sometimes happened close to the squashed flange (i.e. major-axis specimens) and sometimes happened away from the flange in compression (i.e. minor-axis specimens).



Figure 5: All tested specimens: Buckling shape of the specimens

The axial load vs. end shortening response (P- δ) of the specimens is shown in Fig. 6. Fig 6(a) is for applied axial load and minor-axis bending (no. 1-8), Fig. 6(b) shows the results for applied axial load and major-axis bending (no. 9-13) and the case of just axial load (no. 22), and Fig. 6(c) is for axial load and biaxial bending (no. 14-21). The results show the high sensitivity of the beam-column specimen behavior to the magnitude and the position of the eccentric load. This sensitivity was also observed in Phase 1 of the project for lipped channel beam-columns. Initial axial stiffness of the response is a function of eccentricity and this extends in the post-peak range

to the ductility of the response. Specimens having larger eccentricities showed the least strength degradation in the post-peak regime.

The end moment vs. the average end rotation ($M-\theta$) are provided in Fig. 7. Fig 7(a) is for applied axial load and minor-axis bending (no. 1-8), Fig. 7(b) shows the results for applied axial load and major-axis bending (no. 9-13) and the case of axial load alone (no. 22), and Fig. 7(c) is for axial load and biaxial bending (no. 14-21). Note, subscript 1 denotes principal major-axis quantities (M_1, θ_1) and subscript 2 denotes principal minor-axis quantities (M_2, θ_2). The moment(s) are normalized by the principal yield moment(s) and the rotation is the absolute average of the two end rotations. Accordingly, both the left and right sides of the figures show positive rotation, but about different principal axes. Fig. 7(a) verifies that when the eccentricity is about the principal minor-axis (no. 1-8) the response is essentially decoupled behavior and the rotation about the major-axis is negligible. Similar response is observed for the eccentricity about the principal major-axis bending (no. 9-13), where the principal minor-axis rotation is small, especially before reaching the maximum load capacity, as shown in Fig. 7(b). Fig. 7(c) provides the moment-rotation response for the axial load and bi-axial bending cases (no. 14-21) and provides an illustration of the coupled nature of the rotation response. Fig. 7 also reveals that post-peak strength about the principal major-axis typically degrades significantly, while about the minor-axis degradation is typically benign.

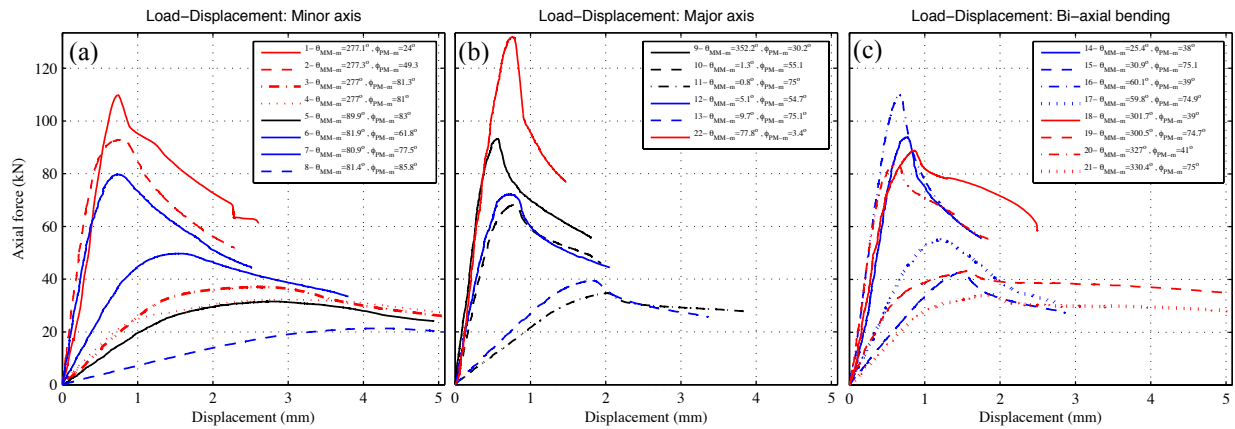


Figure 6: Test results: Load vs. displacement.

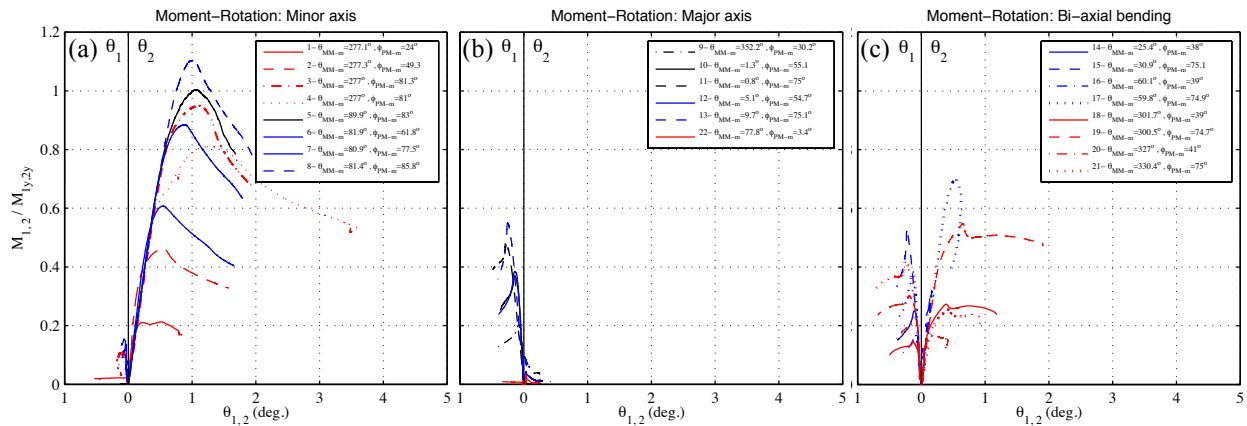


Figure 7: Test results: Normalized end moment vs. end rotation (averaged absolute values)

The twenty-two conducted stub beam-column tests on the specimens having Zee sections provide an approximation for the complete strength interaction surface in the P - M_1 - M_2 space, as shown in Fig. 8. For a structural member already commonly used in steel frame construction (see Fig. 1), the collected set of data provides an excellent evaluation for the accuracy of current beam-column strength prediction methods and the newly proposed beam-column predictions (Torabian et. al. 2013, 2014b).

3. Comparison with AISI-S100-12 beam-column strength predictions

The North American cold-formed steel specification (AISI-S100 2012, section C5.2) employs a simple linear interaction expression for examining beam-column capacity, as follows:

$$\frac{\bar{P}}{\phi_c P_n} + \frac{C_{mx} \bar{M}_x}{\phi_b M_{nx} \alpha_x} + \frac{C_{my} \bar{M}_y}{\phi_b M_{ny} \alpha_y} \leq 1.0 \quad (1)$$

where, \bar{P} , \bar{M}_x , and \bar{M}_y are the required strengths, (demand), and P_n , M_{nx} , M_{ny} and are the nominal strengths (capacity) determined by either Effective width Method (EWM) or Direct Strength Method (DSM). Nominal capacities are converted to available capacity using the resistance factors ϕ_c (typically 0.85) and ϕ_b (typically 0.9) for compression and bending. C_{mx} and C_{my} approximately account for moment gradient effects; and $\alpha_x = 1 - \bar{P}/P_{Ex}$ and $\alpha_y = 1 - \bar{P}/P_{Ey}$ estimate the second-order P - δ moments, where P_{Ex} and P_{Ey} are the Euler buckling loads. Note, x is taken as the principal major-axis (1) and y as the principal minor-axis (2) in the analyses provided herein.

Table 5: Direct strength method calculations for the test specimen at anchor points

Normalized axial strength- DSM ^a				Normalized flexural strength-DSM							
				Major axis bending ^a				Minor axis bending ^a			
P_{cr}^b/P_y^c	P_{crd}/P_y	P_{cre}/P_y		M_{cr}^b/M_{1y}^c	M_{crd}/M_{1y}	M_{cre}/M_{1y}		M_{cr}^b/M_{2y}^c	M_{crd}/M_{2y}	M_{cre}/M_{2y}	
0.18	1.70	3.36		1.07	1.74	14.9		1.48	4.39	367	
λ_{c1}	λ_{cd}	λ_{ce}		λ_{c1}	λ_{cd}	λ_{ce}		λ_{c1}	λ_{cd}	λ_{ce}	
2.21	0.77	0.55		1.01	0.76	0.26		0.82	0.48	0.05	
P_{nl}/P_y	P_{nd}/P_y	P_{ne}/P_y	P_n/P_y	M_{nl}/M_{1y}	M_{nd}/M_{1y}	M_{ne}/M_{1y}	M_{1n}/M_{1y}	M_{nl}/M_{2y}	M_{nd}^d/M_{2y}	M_{ne}/M_{2y}	M_{2n}/M_{2y}
0.43	0.90	0.88	0.43	0.87 ^e	0.94	1.0 ^e	0.87	0.96 ^e	1.25	1.0 ^e	0.96
				0.93 ^f	0.94	1.1 ^f	0.94	1.46 ^f	1.25	1.85 ^f	1.25

^a Direct strength method: AISI-S100-12.

^b Elastic buckling analysis by CUFSM4.06. Generalized boundary condition: C-C.

^c Yield strength. $P_y=266.8$ kN, $M_{1y}=13.8$ kN-m, $M_{2y}=2.19$ kN-m.

^d Inelastic strength per AISI-S100-12.

^e When the local slenderness is greater than 0.776, the inelastic reserve is just ignored, and slenderness is calculated based on the M_{ne} without inelastic reserve.

^f Nominal capacity including inelastic reserve for global buckling capacity M_{ne} and slenderness calculations.

To utilize DSM for the nominal capacity of anchor points with pure axial load and pure principal bending moments (P_n , M_{1n} , M_{2n}), the critical elastic local and distortional buckling axial load and moments were determined using CUFSM 4.06 finite strip program (Schafer and Adany 2006) assuming the end boundary condition as clamped-clamped (C-C). The generalized boundary condition capability in CUFSM 4.06 can directly model the warping fixed end conditions as well

as fixed boundary condition for rotational degrees of freedom at the end of the specimen (Li and Schafer 2010a); however, the signature curve does not exist in this case, and the results are slightly more complex. Consequently, the local and distortional buckling modes may need to be identified manually by visual inspection of the buckling mode shapes. The mode classification capability of CUFSM 4.06 can also help identifying the type of buckling ((Li and Schafer 2010a), but requires use of sharp corner models. Global elastic column buckling and lateral-torsional beam buckling loads were determined from CUTWP (Sarawit 2006). Note, for global flexural buckling the full length between the pins (specimen length, plus 158 mm at each end) was used, and for global torsional buckling due to warping fixity provided by the welded-on end plates, only the specimen length was used.

The normalized elastic buckling loads including, local, distortional and global critical loads for pure axial load and pure principal bending moments (P_n , M_{1n} , M_{2n}) are tabulated in Table 5. Using the elastic critical loads, the associated slenderness values are calculated and implemented to determine the nominal capacity of anchor points per Direct Strength Method in Appendix 1 of AISI-S100-12 specification. The inelastic strength has been considered in the nominal capacities, when applicable.

The software program CFS was employed to determine the nominal strength of the anchor points in accordance with the Effective Width method (CFS 2015). In CFS the Zee section is modeled in the principal coordinate system of the section. Similar to the DSM calculations, the full length between the pins (specimen length, plus 158 mm at each end) was used for global flexural buckling, and due to warping fixity provided by the end plates, again only the specimen length was used for global torsional buckling ($L_m=305$ mm). The results of EWM for P_n , M_{1n} , M_{2n} of the tested specimens were $0.38P_y$, $0.68M_{Iy}$, and $0.96M_{2y}$, respectively.

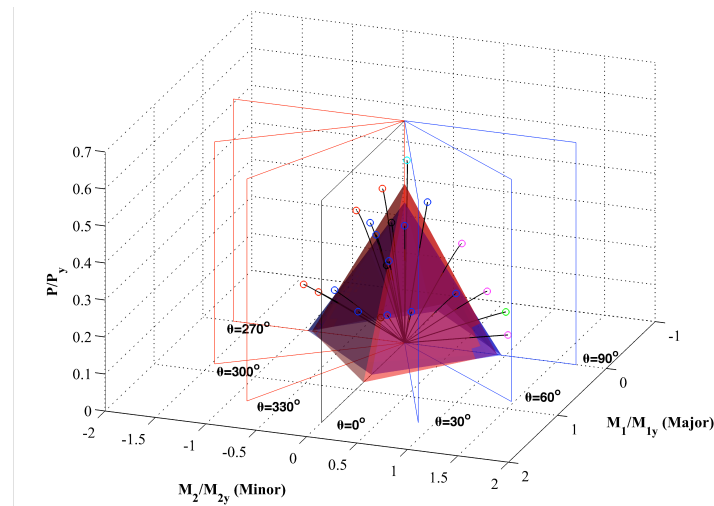


Figure 8: Strength surfaces in P-M₁-M₂ space: Test results (line results), Peak load (clear circles), DSM nominal strength surface (red surface), EWM nominal strength surface (blue surface)

By having the anchor point capacities via both EWM and DSM, the linear interaction equation provided in Eq. (1), is used by setting $C_{mx}=C_{my}=\alpha_x=\alpha_y=\phi_c=\phi_b=1.0$ to develop the nominal strength surface under any combination of demands, and compared to the test data in Figs. 8 and 9. The two methods (EWM and DSM) provide similar interaction surfaces for the specimens.

EWM is more conservative than DSM for axial and major-axis anchor points. The load history of the tests is shown in Figs. 8 and 9 with the normalized ultimate strength marked by open circles. All of the observed ultimate strengths are outside of the interaction surfaces, qualitatively suggesting that the linear interaction equation of the specification is conservative. As shown in Fig. 9, some short specimens, especially in minor-axis bending, were capable of reaching the plastic strength limit state and large inelastic reserve strength was developed in the test results.

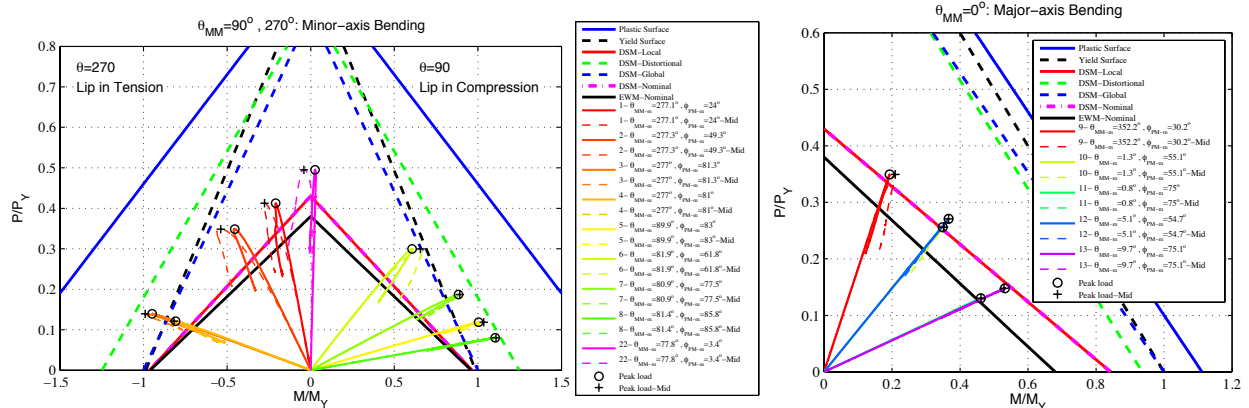


Figure 9: Test results vs. AISI-S100-12-DSM and EWM in principal axes

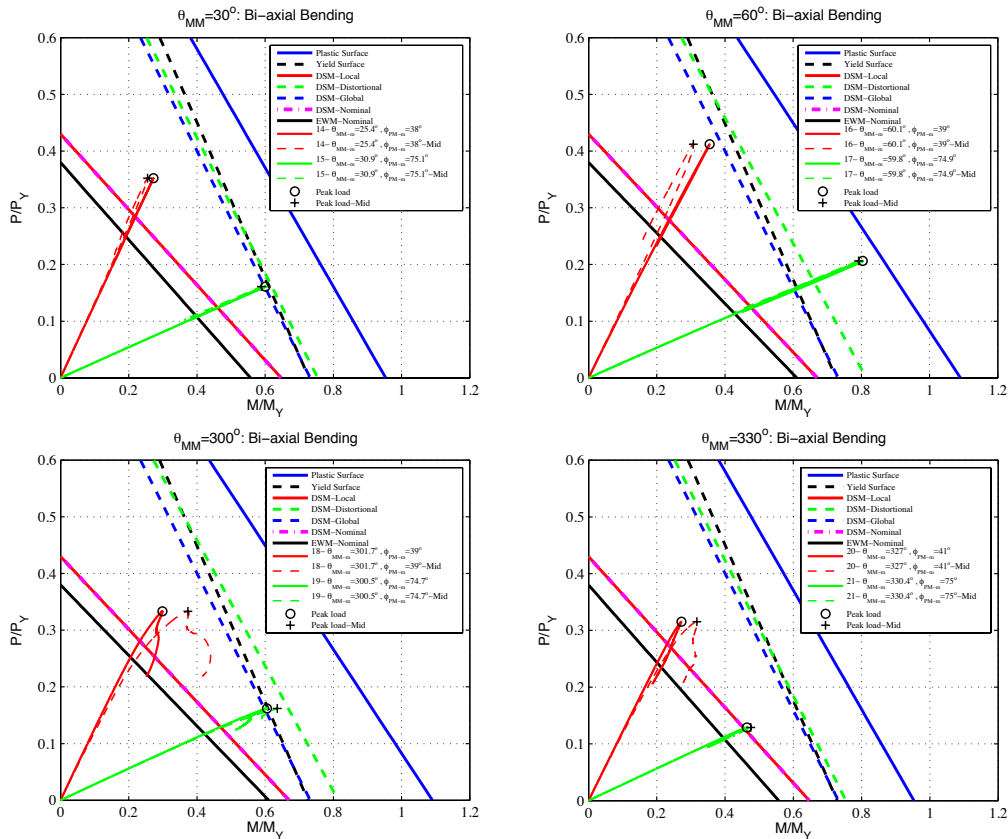


Figure 10: Test results vs. AISI-S100-12-DSM and EWM axes in non-principal axes

β_n per AISI-S100-12 utilizing DSM and EWM is calculated from the interaction surfaces and compared against the single parameter normalized strength, β_{Test} , in Table 6. The average test to

predicted ratios $\beta_{Test}/\beta_{n-EWM}$ and $\beta_{Test}/\beta_{n-DSM}$ are 1.41, and 1.29, respectively, and the associated CoVs are 12.3%, and 15.6%. Reliability analysis based on these statistics is provided in the following section.

Table 6: AISI-S100-12-DSM and EWM strength predictions for test specimens at the ultimate strength

Loading condition	Measured		at peak load		Test	AISI-S100-12		Comparison	
	θ_{MM-m} (deg.)	Φ_{PM-m} (deg.)	θ_{MM-f} (deg.)	Φ_{PM-f} (deg.)	β_{Test}	β_{n-EWM}	β_{n-DSM}	$\beta_{Test}/\beta_{n-EWM}$	$\beta_{Test}/\beta_{n-DSM}$
1	277.1	24.0	277.1	24.0	0.46	0.46	0.36	1.34	1.20
2	277.3	49.3	277.3	49.3	0.58	0.58	0.40	1.47	1.34
3	277.0	81.3	277.0	81.3	0.97	0.97	0.64	1.51	1.43
4	277.0	81.0	277.0	81.0	0.82	0.82	0.64	1.30	1.23
5	89.9	83.0	89.9	83.0	1.01	1.01	0.73	1.36	1.32
6	81.9	61.8	81.9	61.8	0.68	0.68	0.45	1.53	1.41
7	80.9	77.5	80.9	77.5	0.91	0.91	0.58	1.61	1.50
8	81.4	85.8	81.4	85.8	1.12	1.12	0.70	1.60	1.52
9	352.2	30.2	352.2	30.2	0.41	0.41	0.35	1.25	1.08
10	1.3	55.1	1.3	55.1	0.45	0.45	0.42	1.22	1.02
11	0.8	75.0	0.8	75.0	0.51	0.51	0.56	1.06	0.86
12	5.1	54.7	5.1	54.7	0.47	0.47	0.41	1.31	1.10
13	9.7	75.1	9.7	75.1	0.58	0.58	0.51	1.29	1.07
14	25.4	38.0	25.4	38.0	0.45	0.45	0.34	1.42	1.23
15	30.9	75.1	30.9	75.1	0.63	0.63	0.46	1.52	1.30
16	60.1	39.0	60.1	39.0	0.54	0.54	0.35	1.65	1.47
17	59.8	74.9	59.8	74.9	0.82	0.82	0.48	1.84	1.65
18	301.7	39.0	301.7	39.0	0.45	0.45	0.35	1.37	1.22
19	300.5	74.7	300.5	74.7	0.65	0.65	0.48	1.44	1.29
20	327.0	41.0	327.0	41.0	0.43	0.43	0.34	1.35	1.18
21	330.4	75.0	330.4	75.0	0.51	0.51	0.46	1.22	1.05
22	77.8	3.4	77.8	3.4	0.50	0.50	0.39	1.34	1.19
							Mean	1.41	1.26
							Std	0.17	0.19
							C.O.V	12.3%	15.1%

4. Reliability analysis

A reliability-based method per Chapter F of the AISI-S100-12 is utilized to quantitatively evaluate the AISI-S100-12 predictions including both EWM and DSM. Accordingly, the reliability index β_o is determined against the test results. (Note, reliability index β_o should not be confused with the normalized single parameter strength, β).

The resistance factor ϕ is calculated as follows (AISI-S100 2012):

$$\phi = C_\phi (M_m F_m P_m) e^{-\beta_o \sqrt{V_m^2 + V_F^2 + C_r V_P^2 + V_Q^2}} \quad (2)$$

where, C_ϕ , the calibration factor is 1.52; M_m is the mean value of the material factor ($M_m = 1.05$ for combined axial load and bending); F_m is the mean value of the fabrication factor ($F_m = 1.00$ for combined axial load and bending); P_m is the mean value of the professional factor (P_m is the

mean of the test-to-predicted ratios per Table 7); β_o is the target reliability index, which is assumed to be 2.5 for structural members (AISI-S100 2012); V_m is the coefficient of variation of the material factor ($V_m = 0.10$ for combined axial load and bending); V_F is the coefficient of variation of the fabrication factor ($V_F = 0.05$ for combined axial load and bending); the sample size C_P value is assumed to be 1.0; V_P is the coefficient of variation of the professional factor (here V_P is the coefficient of variation of the test-to-predicted ratios per Table 7); and V_Q is coefficient of variation of the load effect ($V_Q=0.21$ for standard analyses). See Meimand and Schafer (2014) for a complete discussion of this reliability formulation.

In Table 7, the reliability index is back-calculated from Eq. 2 for two different resistance factors (0.85 typical of columns and 0.90 typical of beams); and the resistance factor is also calculated based on the member target reliability of 2.5. The reliability analyses reveal that the current beam-column design methods in AISI-S100-12 are significantly conservative for the studied member. Notably, the same results were achieved for lipped channel specimens in the previous studies (Torabian et al. 2015). Taking all data points into account, the calculated reliability indices for DSM method are 3.10 ($\phi=0.85$) and 2.90 ($\phi=0.90$), and for EWM they are 3.63 ($\phi=0.85$) and 3.42 ($\phi=0.90$), as also tabulated in Table 7.

As the reliability analysis of the anchor points is not emphasized in this study, the reliability indices for the DSM method, excluding specimens no. 11, 13, and 22 which are close to the anchor points, are 3.30 ($\phi=0.85$) and 3.09 ($\phi=0.90$), and for EWM they are 3.55 ($\phi=0.85$) and 3.77 ($\phi=0.90$), as shown in Table 7. The reliability indices are significantly larger than the target reliability index of 2.5, therefore significant potential for improvement of the current AISI-S100-12 specification methods for beam-columns exists. This result is the motivation for an ongoing study on a new DSM approach for beam-columns, which considers the actual stress distribution on the cross-section in the strength prediction.

Table 7: Reliability analysis of the direct strength and effective width method

Method	No. of spec.	P_m	V_p	$\beta_o(\phi=0.85)$	$\beta_o(\phi=0.9)$	$\phi(\beta_o=2.5)$
Direct strength method	Non-Anchors ^a (18)	1.29	0.13	3.25	3.04	1.04
	All (22)	1.26	0.15	3.05	2.85	0.99
Effective width method	Non-Anchors ^a (18)	1.44	0.11	3.77	3.55	1.19
	All (22)	1.41	0.12	3.63	3.42	1.15

^aexcluding specimens no. 11, 13, and 22

5. Summary and Conclusions

An experimental program including twenty-two Zee shaped beam-columns, 700Z225-60 ($F_y=550\text{MPa}$) at the length of 305mm, was used to evaluate current AISI-S100-12 specification predictions for beam-column strength, including EWM and DSM. The selected cross-section was tested to fully explore the beam-column performance under axial compressive load and any combination of major- and minor-axis bending. It is found that the cross-sectional applied stress distribution is the most important parameter in modulating the failure mechanisms, such as local or distortional buckling. In addition, the member ductility is strongly correlated to the degree of eccentricity in the axial load, and axial load on the member. Comparing the results to the current

AISI-S100-12 specification predictions indicate that both the effective width method (EWM) and direct strength method (DSM) are conservative as currently applied. This is due to the use of a simple linear interaction strength expression in AISI-S100-12 and the fact that both EWM and DSM predict conservative “anchor points” for isolated axial load and major-axis and minor-axis bending of the studied cross-section. A method that directly considers the stability and strength under the actual applied actions is currently under development by the authors. The new DSM for beam-columns is intended to improve the current strength prediction in AISI-S100-12.

Acknowledgments

The authors would like to acknowledge the American Iron and Steel Institute and the Metal Building Manufacturers Association for funding this study. In addition, we would like to acknowledge BlueScope buildings for donating specimens and Frazier Company for donating the external support rack. We would also like to thank Senior Technician Nickolay Logvinovsky for his assistance with the experimental setup, and Xi Zhao, Austin Lee, Bo Harwood, Caroline Slattery, and John Boutillier for their assistance with the non-contact geometric measurements and preparation of the specimens. Any opinions, findings, and conclusions or recommendations expressed in this material are those of the authors and do not necessarily reflect the views of the sponsors or other participants.

References

- AISI-S100 (2012). “North American Specification for the design of cold-formed steel structural members.” Washington (DC, USA): *American Iron and Steel Institute*.
- A370-12a. (2012). “Standard Test Methods and Definitions for Mechanical Testing of Steel Products.” American Society for Testing and Materials (ASTM). Philadelphia.
- CFS 8.05. (2015). *RSG Software, Inc.* <http://www.rsgsoftware.com>.
- Kalyanaraman V, Jayabalan P. (1994). Local buckling of stiffened and unstiffened elements under nonuniform compression. *Twelfth International Specialty Conference on Cold-Formed Steel Structures*.
- Li, Z., Schafer, B.W. (2010a). “Buckling analysis of cold-formed steel members with general boundary conditions using CUFSM: conventional and constrained finite strip methods.” *Twentieth International Specialty Conference on Cold-Formed Steel Structures*. Saint Louis, Missouri, USA, November 3 - 4.
- Li, Z., Schafer, B.W. (2010b). “Application of the finite strip method in cold-formed steel member design.” *Journal of Constructional Steel Research*, 66 971–980.
- Loh, T.S. (1985). “Combined axial load and bending in cold-formed steel members”. *PhD Thesis*. Cornell University, Ithaca.
- Meimand V. Z., Schafer B.W. (2014). “Impact of load combinations on structural reliability determined from testing cold-formed steel components.” *Structural Safety*. 48, 25-32.
- Miller, T.H., Pekoz, T. (1994). “Load-Eccentricity effects on cold-formed steel lipped-channel columns.” *Journal of Structural Engineering*, 120(3) 805–823.
- Pekoz, T. (1986). “Development of a unified approach to the design of cold-formed steel members.” *Eighth International Specialty Conference on Cold-Formed Steel Structures*, St. Louis, MO. 77–84.
- Prime. (2015). Web page: <http://www.Primesteelbuildings.com>.
- Sarawit, A. (2006) “CUTWP thin-walled section properties”, December 2006 update. (<http://www.ce.jhu.edu/bschafer/cutwp>).
- Schafer, B.W., Adany, S. (2006). “Buckling analysis of cold-formed steel members using CUFSM: Conventional and Constrained Finite Strip Methods.” *Proceedings of the eighteenth international specialty conference on cold-formed steel structures*. 39–54. (<http://www.ce.jhu.edu/bschafer/cufsm>)
- Schafer, B.W., Adany S. (2006). “Buckling analysis of cold-formed steel members using CUFSM: Conventional and Constrained Finite Strip Methods. *Eighteenth international specialty conference on cold-formed steel structure*. Orlando, FL, United States: University of Missouri-Rolla, Rolla, MO, United States.
- Shifferaw, Y. (2010). “Section capacity of cold-formed steel members by the Direct Strength Method. *PhD Thesis*. Johns Hopkins University, Baltimore.

- Torabian S., Zheng B., Schafer B.W. (2013). "Direct Strength Prediction of Cold-Formed Steel Beam-Columns", *Thin-walled Structures Group at The Johns Hopkins University. American Iron and Steel Institute (AISI)*. (<http://www.ce.jhu.edu/bschafer/dsmbeamcol/>)
- Torabian, S., Zheng, B., Schafer, B.W. (2014a) "Experimental study and modeling of cold-formed steel lipped channel stub beam-columns." *Annual Stability Conference Structural Stability Research Council*, Toronto, Canada, March 25-28.
- Torabian, S., Zheng, B., Schafer, B.W. (2014b) "Reliability of the new DSM beam-column design method for cold-formed steel lipped channel." *22nd International Specialty Conference on Cold-Formed Steel Structures*. St. Louis, Missouri, USA, November 5-6.
- Torabian, S., Zheng B., Schafer, B.W. (2015). "Experimental response of cold-formed steel lipped channel beam-columns." *Thin-Walled Structures*, 89 152-168.
- Yiu F, Pekoz T. (2000). "Design of Cold-Formed Steel Plain Channels." *Fifteenth International Specialty Conference on Cold-Formed Steel Structures*, St. Louis MO. 13–22.